

UWB Multistatic Radars for Obstacle Detection and Imaging in Railroad Crossing Areas

(Invited Paper)

Marco Govoni^{*†}, Francesco Guidi[†], Enrico M. Vitucci[†],
Vittorio Degli Esposti[†], Giovanni Tartarini[†] and Davide Dardari[†]

^{*} Direzione Tecnica Standard Tecnologici e Sperimentali
Rete Ferroviaria Italiana (RFI) SpA, Rome, Italia

Email: m.govoni@rfi.it

[†]Department of Electrical and Information Engineering (DEI),
University of Bologna, Bologna, Italy

Email: {f.guidi, enricomaria.vitucci, giovanni.tartarini, v.degliesposti, davide.dardari}@unibo.it

Abstract—Multi-static radars exploiting the ultrawide-band (UWB) technology represent a promising solution to improve the safety of rail crossing surveillance areas in case of entrapped vehicles. In particular, by taking advantage of the large bandwidth, location and volume information about the obstacles can be obtained. To this purpose, we propose a hybrid approach combining the multi-static radar and mono-static imaging scanner concepts able to detect and localize the obstacle, as well as to roughly estimate its volume and shape, thus avoiding the deployment of moving transmitters or a large amount of antennas. The 3D imaging and volume estimation capabilities of the proposed solution are assessed using ray tracing simulations of the rail crossing surveillance area.

Index Terms—Ultra-wide band, multi-static UWB radar, railroad crossings, imaging

I. INTRODUCTION

Level crossings are dangerous areas where railways intersect the road traffic, and the entrapment of obstacles like vehicles can cause serious damage to trains and its passengers. To increase their safety, surveillance systems able to detect obstacles are receiving a growing interest by rail operators.

In recent years several systems have been proposed, each supported by a different technology: mono-static UWB radars studied in [1], Lidars are exploited in [2] through a single-head 3D laser range finder, whereas stereo cameras are investigated in [3]. Unfortunately, these solutions present some limitations: in the former, two sensors monitor the area and detect obstacles by exploiting the backscattered signal, but no information is available relating the obstacle volume and position. On the other side, the laser solution adopts only one eye-device to monitor the area with high-resolution, but heavy weather conditions (e.g., fog) might cause false alarms or even a system failure. The same applies for camera-based systems.

According to current regulations, level crossing surveillance systems must satisfy functional requirements in terms of obstacle volume recognition, robustness to weather conditions, cost, and easy installation on existing infrastructures, making their design challenging. Specifically, the key performance parameter is the capability to discriminate the obstacle volume

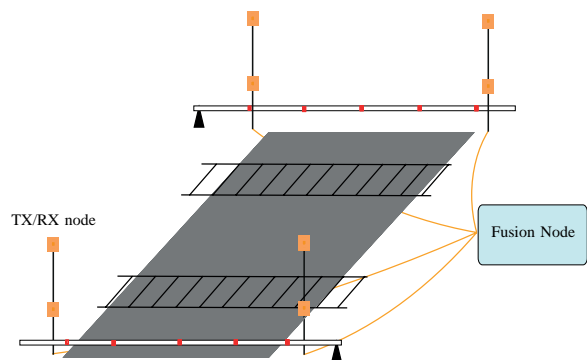


Fig. 1. The level crossing surveillance system.

(when present), as only obstacles larger than one cubic meter must generate an alarm with consequent stop of the train.¹ Therefore, level crossing surveillance systems are requested to implement also some rough 3D imaging capability.

The UWB multi-static radar is considered a promising technology for surveillance systems able to provide both detection and localization functionalities. Unfortunately, in rail crossings the potentially large size of obstacles prevent from the adoption of classical signal processing techniques that are implicitly based on unrealistic assumptions such as isotropic scattering, moving objects, and punctual obstacle size [4]. On the other hand, mono-static UWB imaging systems (UWB scanners) provide high-accuracy obstacle imaging but require a large amount of antennas mounted on a mechanical arm that circumnavigates the obstacle contour, which is not feasible for the application under consideration [5].

In this paper, a UWB partial multi-static radar for railway crossings surveillance capable of detecting, localizing and estimating the obstacle volume, even in static conditions, is presented. It makes use of a fixed set of UWB nodes to obtain the information about the volume of the obstacle thus discriminating between large or small obstacles (see

¹This requirement holds, for instance, for the Italian rail operator *Rete Ferroviaria Italiana (RFI)*.

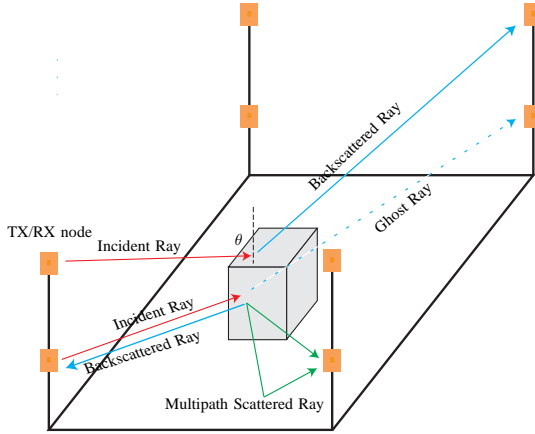


Fig. 2. Path loss experienced by nodes when the signal is backscattered by the obstacle

Fig. 1). The proposed system, namely fixed object scanner (FOS), performs a sequence of scanning phases where only suitable subsets of nodes participate to the measurement of the environment response (backscatter) to the UWB interrogation signals emitted by nodes themselves. All measurements are successively collected by a fusion node responsible for taking an overall decision on the event. To reduce the number of level crossings to be monitored by a given fusion center, an interesting opportunity is to connect the sensors and the fusion center through fiber optic links. Within this perspective, the possibility to exploit the UWB-over-Fiber technology is under investigation [6]. Note that can be considered as an hybrid approach combining the UWB multi-static radar and the mono-static imaging scanner configurations. As a consequence, it allows for gaining some of the advantages of both configurations and mitigating their drawbacks. Indeed, it overcomes the limitations of optical based systems [2], [3] and, at the same time, offers good obstacle detection and localization performance inside the level crossing.

II. THE FOS IMAGING ALGORITHM

The surveillance system investigated is composed of a set of transmitter (TX) and receiver (RX) nodes, located at different heights at the vertices of the monitored area, as shown in Fig. 1. As it will be described later, the sounding of the environment via UWB interrogation signals and subsequent analysis of backscattered signals is split in different phases to which only a subset of nodes participate leading to a partial multi-static radar configuration. In addition, with the purpose to facilitate the 3D imaging algorithm described later, the monitored area is subdivided into N_{pixel} 3D cubic pixels of side Δ . The 3D imaging process of the obstacle can be summarized in the following steps: clutter removal, pixel detection, imaging, and volume estimation.

A. Signal Model

Denote with \mathcal{A}_p the set of transmitters and receivers pairs which are active during the phase p , with $p \in \{A, B, C, D, E\}$

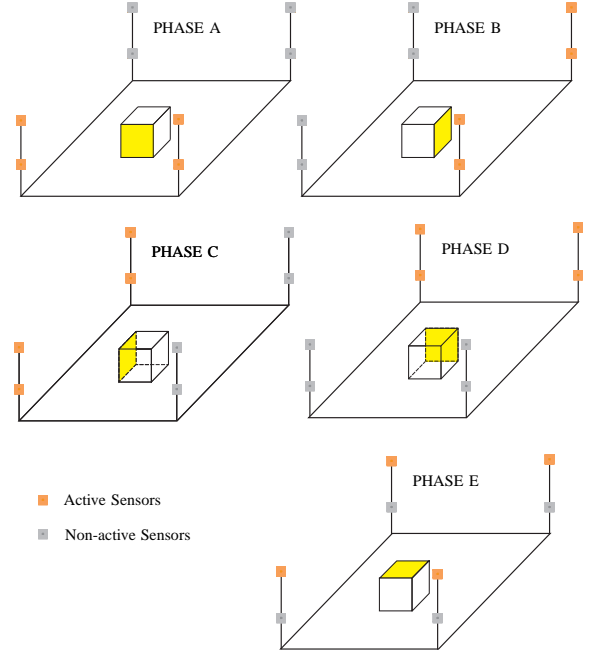


Fig. 3. Active sensors depending on the phase p considered on FOS algorithm.

as shown in Fig. 3. To avoid inter-nodes interference a time division multiple access (TDMA) approach is considered where only one node is transmitting and the others are receiving. Consider, without loss of generality, the active transmitter sends an interrogation UWB pulse $g(t)$. Note that in actual UWB systems, to overcome the low emission power imposed by regulatory issues, a sequence of N_p pulses is usually transmitted to allow the receiver for collecting more energy. In case of coherent receivers, our analysis considering the transmission of a single pulse is equivalent to that of multiple pulses if a noise power reduction of N_p is taken into account (processing gain).

The signal backscattered by the environment and received by the RX node of the i th pair, with $i \in \mathcal{A}_p$, is

$$r_i(t) = s_i(t) + n_i(t) \quad (1)$$

where $s_i(t)$ is the useful signal component and $n_i(t)$ is the additive white Gaussian noise (AWGN). The useful component can be further decomposed into a sum of contributions (if any) coming from all the 3D pixels the area has been subdivided into. Specifically, it can be written

$$s_i(t) = \sum_{k=1}^{N_{\text{pixel}}} a_i^{(k)} \cdot p_i^{(k)}(t - \tau_i^{(k)}) \quad (2)$$

with $\tau_i^{(k)}$ being the transmitter-pixel-receiver time-of-flight of the signal, and $p_i^{(k)}(t)$ being the channel response to $g(t)$ (if present) due to the k th pixel including also the multipath. The term $a_i^{(k)}$ accounts for the total path loss, that is

$$a_i^{(k)} = \begin{cases} 0 & \text{empty or shadowed pixel} \\ \frac{1}{\sqrt{PL_i^{(k)}}} & \text{otherwise} \end{cases} \quad (3)$$

having defined $PL_i^{(k)} = PL_{TX,i}^{(k)} \cdot PL_{RX,i}^{(k)} \cdot \sigma_i^{(k)}$ the total path loss experienced by the two nodes, where $PL_{TX,i}^{(k)}$ and $PL_{RX,i}^{(k)}$ are the attenuations due to the free-space propagation between the TX and the obstacle, and the obstacle and the RX, respectively. $\sigma_i^{(k)}$ accounts for the obstacle reflection coefficient related to the part of the obstacle falling in the k th pixel, and it is strictly linked to the angle θ formed by the incident and the backscattered waves. In Fig 2 all propagation phenomena involved in the interrogation phase are illustrated. Note that typically only rays with $\theta < 90^\circ$ (blue line) are reflected. This aspect will be taken into account in the 3D imaging algorithm described later.

Signals are successively sampled, with sampling time t_s , in N time instants t_1, t_2, \dots, t_N belonging to an observation interval containing all the useful received components, leading to

$$\mathbf{r}_i = \mathbf{s}_i + \mathbf{n}_i \quad (4)$$

with $\mathbf{r}_i = [r_{i,1}, r_{i,2}, \dots, r_{i,N}]^T = [r_i(t_1), r_i(t_2), \dots, r_i(t_N)]^T$ and similarly for \mathbf{s}_i and \mathbf{n}_i . Each component of vector \mathbf{n}_i is a zero mean Gaussian random variable (RV) with variance σ^2 .

B. Clutter Removal and Ghost Effect Mitigation

An important issue when detecting the presence of steady obstacles is the static environment response (*static clutter*) caused, for example, by the rail and poles. This component is removed by using an *empty-room* approach [7] in which the reference signals $\check{\mathbf{r}}_i$, recorded in the absence of obstacles, are subtracted from the actual received signals. Note that when an obstacle is present, part of the static clutter could be hidden leading to imperfect clutter suppression (see Fig 2). To counteract this *ghost effect*, only the signal components corresponding to positive variations in the received energy are taken into account during the clutter removal process.

In particular, for each sampled version of the received signal, we have

$$\begin{cases} \mathbf{r}_i = \mathbf{r}_i - \check{\mathbf{r}}_i & \text{if } |\mathbf{r}_i|^2 \geq |\check{\mathbf{r}}_i|^2 \\ \mathbf{r}_i = 0 & \text{if } |\mathbf{r}_i|^2 < |\check{\mathbf{r}}_i|^2 \end{cases} \quad (5)$$

where $|\mathbf{r}|^2$ means element wise square operation.

C. 3D Image Formation

In classical multi-static radar schemes, the backscattered response to the UWB interrogation signals sent by the transmitters is collected by all nodes and jointly processed by the localization algorithm. However, the finite size and the anisotropic scattering of the obstacle might prevent some nodes (e.g., those located in the opposite direction) from receiving the backscattered signal, differently from that expected by the multi-static radar algorithm (for example, in Fig 2 the ray represented by the dashed blue line). This generates, in addition to multipath components, serious ambiguities in imaging formation and localization that might not be solved. To overcome such limitation, we consider a partial multi-static radar system which alternatively activates each side of the monitored area, as shown in Fig. 3. In particular, the proposed

FOS algorithm performs 5 phases, 4 for the lateral sides and one for the top of the area. During each phase p , only the TX-RX pairs located in the considered side are activated and are included in the set \mathcal{A}_p thus miming mono-static imaging scanners with fixed nodes. In this way the resulting partial multi-static radar operates most likely in conditions where $\theta < 90^\circ$ is satisfied, with a consequent significant mitigation of the aforementioned ambiguities during the imaging process.

Obstacle detection and image formation consist in checking whether the generic pixel is a candidate for containing part of the obstacle (if present). This can be accomplished by performing during phase p and for each pixel k , with $k = 1, 2, \dots, N_{\text{pixel}}$, the following binary detection test with unpredictable sign

$$\begin{cases} \mathbf{r}_i^{(k)} = \mathbf{n}_i & \mathcal{H}_0 \\ \mathbf{r}_i^{(k)} = \pm a_i^{(k)} \tilde{\mathbf{g}}_i^{(k)} + \mathbf{n}_i & \mathcal{H}_1 \end{cases} \quad (6)$$

$\forall i \in \mathcal{A}_p$, having defined

$$\tilde{\mathbf{g}}_i^{(k)} = [g(t_1 - \tau_i^{(k)}), g(t_2 - \tau_i^{(k)}), \dots, g(t_N - \tau_i^{(k)})]^T \quad (7)$$

the expected received signal template delayed by time-of-flight $\tau_i^{(k)}$. The probability distribution functions (p.d.f.s) of the composite received signal $\mathbf{r}^{(k)} = \left[\left\{ \mathbf{r}_i^{(k)} \right\}_{i \in \mathcal{A}_p} \right]$ under \mathcal{H}_0 and \mathcal{H}_1 can be written, respectively, as

$$\begin{aligned} P(\mathbf{r}^{(k)} | \mathcal{H}_0) &= \prod_{i \in \mathcal{A}_p} K \exp \left(-\frac{\sum_{n=1}^N (r_{i,n}^{(k)})^2}{2\sigma^2} \right) \quad (8) \\ P(\mathbf{r}^{(k)} | \mathcal{H}_1) &= \prod_{i \in \mathcal{A}_p} \frac{K}{2} \left[\exp \left(-\frac{\sum_{n=1}^N (r_{i,n}^{(k)} - a_i^{(k)} \tilde{g}_{i,n}^{(k)})^2}{2\sigma^2} \right) \right. \\ &\quad \left. + \exp \left(-\frac{\sum_{n=1}^N (r_{i,n}^{(k)} + a_i^{(k)} \tilde{g}_{i,n}^{(k)})^2}{2\sigma^2} \right) \right] \quad (9) \end{aligned}$$

with K being a constant whose value does not affect the test.

The log-likelihood ratio (LLR) based on (8) e (9) can be written as

$$\begin{aligned} \ln \Lambda^{(k)} &= -\frac{1}{2\sigma^2} \sum_{i \in \mathcal{A}_p} \sum_{n=1}^N (a_i^{(k)} \tilde{g}_{i,n}^{(k)})^2 \\ &\quad + \sum_{i \in \mathcal{A}_p} \ln \cosh \left(\frac{1}{\sigma^2} \sum_{n=1}^N r_{i,n}^{(k)} a_i^{(k)} \tilde{g}_{i,n}^{(k)} \right). \quad (10) \end{aligned}$$

To simplify the implementation of the test, the nonlinear function $\ln \cosh(\cdot)$ can be approximated as

$$\ln \cosh(x) = \begin{cases} |x| - \ln 2, & \text{if } |x| \gg 1 \\ x^2/2, & \text{if } |x| \ll 1 \end{cases}.$$

Finally we can write the LLR test as follows

$$\sum_{i \in \mathcal{A}_p} \frac{1}{\sigma^2} \left| \sum_{n=1}^N r_{i,n}^{(k)} a_i^{(k)} \tilde{g}_{i,n}^{(k)} \right| \underset{\mathcal{H}_0}{\overset{\mathcal{H}_1}{\gtrless}} \ln \xi + \sum_{i \in \mathcal{A}_p} \sum_{n=1}^N \frac{(a_i^{(k)} \tilde{g}_{i,n}^{(k)})^2}{2\sigma^2} \quad (11)$$

when $\frac{1}{\sigma^2} \left| \sum_{n=1}^N r_{i,n}^{(k)} a_i^{(k)} \tilde{g}_{i,n}^{(k)} \right| \gg 1$ and, in the opposite case, the approximation becomes

$$\sum_{i \in \mathcal{A}_p} \frac{1}{\sigma^2} \left(\sum_{n=1}^N r_{i,n}^{(k)} a_i^{(k)} \tilde{g}_{i,n}^{(k)} \right) \underset{\mathcal{H}_0}{\overset{\mathcal{H}_1}{\gtrless}} \ln \xi + \sum_{i \in \mathcal{A}_p} \sum_{n=1}^N \frac{(a_i^{(k)} \tilde{g}_{i,n}^{(k)})^2}{2\sigma^2}. \quad (12)$$

Note that in both cases ξ is set according to the Neyman-Pearson criterion in order to guarantee a certain probability of false alarm, which is the probability to detect an object even if it is not present in the monitored area [8]. The system has an overall false alarm probability from which derive the false alarm probability for each pixel which provides the threshold value.

As stated before, this procedure is repeated for each pixel and phase. In the end, all binary test outputs are combined to form the 3D image. In particular, the presence of part of an obstacle in a 3D pixel is detected if at least one LLR was successful during the scanning phases.

D. Obstacle Volume Estimation

The result of the 3D image formation described in the above section is used as input for volume computation to understand obstacle size when it is present and generate an alarm to stop train if the post-processing returns a value greater than 1 cubic meter. Two methods of volume computation are provided:

- average sphere volume computation (ASVC)
- average parallelepiped volume computation (APVC).

The common step of these two approaches is to find the centroid of illuminated pixels. Assuming that the FOS algorithm returns the set $\mathbf{i}_1, \dots, \mathbf{i}_M$ of illuminated pixels, where $\mathbf{i}_i = [x_i \ y_i \ z_i]$, the centroid coordinates $\mathbf{c} = [c_x \ c_y \ c_z]$ are computed as

$$\begin{aligned} c_x &= \frac{1}{M} \sum_{i=1}^M x_i \\ c_y &= \frac{1}{M} \sum_{i=1}^M y_i \\ c_z &= \frac{1}{M} \sum_{i=1}^M z_i \end{aligned} \quad (13)$$

with M being the cardinality of the set. Once the centroid coordinates are evaluated, the ASVC method computes the volume of a sphere centered in \mathbf{c} with radius R equal to the average pixels distance, that is

$$R = \frac{1}{M} \sum_{i=1}^M \|\mathbf{i}_i - \mathbf{c}\|. \quad (14)$$

The APVC method creates, instead, a parallelepiped centered in \mathbf{c} with sides

$$\begin{aligned} \Delta x &= \frac{2}{M_{BC}} \sum_{i=1}^{M_{BC}} |x_i - c_x| \\ \Delta y &= \frac{2}{M_{AD}} \sum_{i=1}^{M_{AD}} |y_i - c_y| \\ \Delta z &= \frac{2}{M_E} \sum_{i=1}^{M_E} |z_i - c_z|. \end{aligned} \quad (15)$$

where M_{BC} is the subset cardinality of illuminated pixel coming from the union of phases B and C of FOS algorithm used to determine the x side of the parallelepiped. Similarly for the subset coming from the union of phases A and B to determine y component (M_{AD}) and phase E to z component (M_E).

III. SIMULATION RESULTS

In order to evaluate the effect of a single obstacle placed in different positions within the area between the barriers, a system configuration composed of $N_{TX} = N_{RX} = 8$ nodes, four at height of 3 m and four at 0.8 m, has been considered as shown in Fig. 2. The surveillance area is divided in 3-D pixels of side $\Delta = 10$ cm and the overall false alarm probability is set to $P_{FA} = 10^{-3}$. The channel transfer function between each TX–RX pair has been simulated with the aid of the 3D ray tracing (RT) software described in [9]. In addition to specular reflection and edge/corner diffraction, modeled through geometrical optics (GO) and uniform theory of diffraction (UTD), the RT tool accounts for the effect of diffuse scattering, modeled through the effective roughness (ER) approach. One of the main parameters of the ER model is the scattering parameter S , which accounts for the amount of the incident power diffused in all directions at the expenses of specular reflection, due to the presence of surface and volume irregularities. The obstacle is modeled as a metal box, whereas ground, barriers, tracks and antenna poles are modeled as slabs. Successively, the UWB channel responses obtained for each TX–RX couple are convoluted in time with a root-raised cosine pulse compliant with the FCC mask in the 3 – 5 GHz band. The 3D imaging approach previously described has been validated with obstacles having volume 5.83, 1, 0.34 m^3 placed inside the surveillance area.

Figure 4 shows the 3D image output of the FOS algorithm when a metal box of 5.72 m^3 , modeled with scattering parameter $S = 0.3$, is located in the middle of the area. The green line represents the real position of the obstacle in RT simulations. As can be noticed, the illuminated pixels match well with the obstacle contour, apart from a small set of outliers pixels. The yellow sphere juxtaposed is derived from the ASVC method whose volume can be taken as representative of the actual volume of the obstacle.

For comparison, the same simulation set up has been used to derive the results in Fig. 5 where the classical UWB multi-static radar approach is considered. Even though the presence

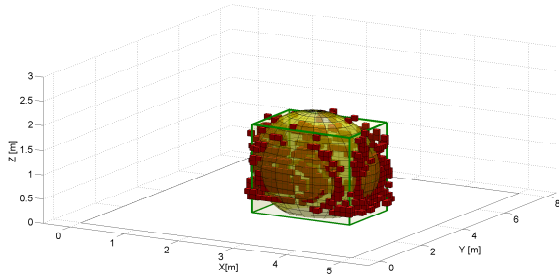


Fig. 4. 3D image of a metal box of 5.83 m^3 in the middle of the surveillance area. ASVC method.

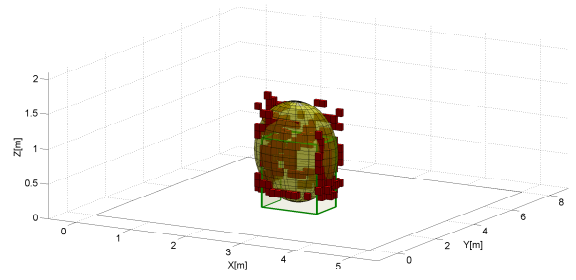


Fig. 7. 3D image of a metal box of 1 m^3 in the middle of the surveillance area. ASVC method.

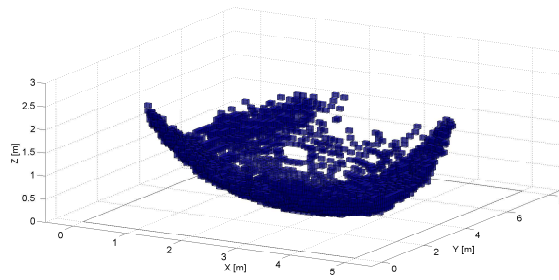


Fig. 5. 3D image of a metal box of 5.83 m^3 in the middle of the surveillance area using the classic UWB multi-static radar approach.

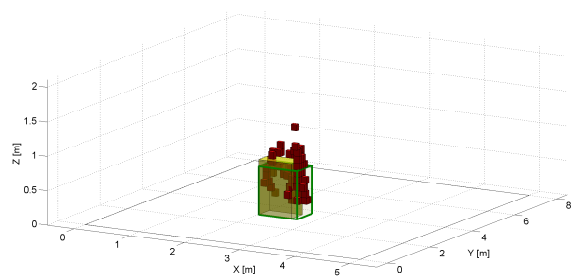


Fig. 8. 3D image of a metal box of 0.34 m^3 in the middle of the surveillance area. APVC method.

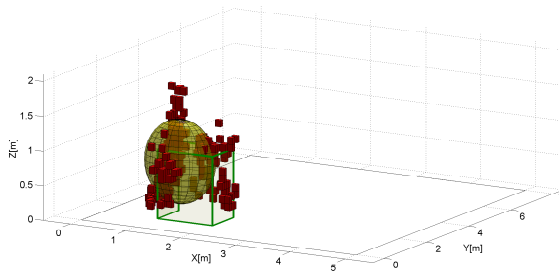


Fig. 6. 3D image of a metal box of 1 m^3 in the corner of the surveillance area. ASVC method.

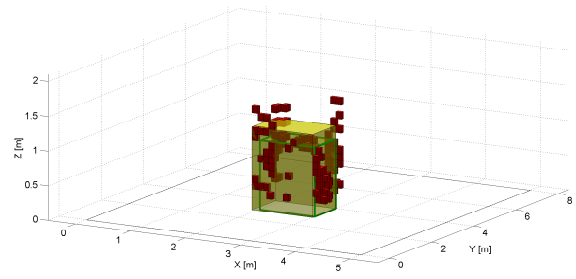


Fig. 9. 3D image of a metal box of 1.00 m^3 in the middle of the surveillance area with scattering $S = 0.2$. APVC method.

of the obstacle is detected, the a huge number of outlier pixels arise due to ambiguities, thus making impossible a realistic volume computation and/or localization of the obstacle. Comparing with 4, the gain introduced by the proposed FOS algorithm is evident.

Figs. 6 and 7 report the results for a metal box of volume 1.00 m^3 (critical volume set by regulation) placed in the lower corner on the left and in the middle of the area, respectively. The proposed FOS algorithm allows for the location of the obstacle in different positions as well as its 3D imaging.

Successively, a metal box of volume 0.34 m^3 , which is below the critical volume value, is placed in the middle of the area, as shown in Fig. 8. As can be seen, the FOS algorithm is still capable of providing a 3D image with small objects.

To understand the effect of different scattering properties of

the obstacle, Fig. 9 reports the results of FOS when an obstacle of critical volume with $S = 0.2$ is present in the middle of the area. In this case our approach is still capable of detecting and locating the obstacle despite the total number of illuminated pixels compared with Fig. 7 is diminished due to the reduction of the total scattered power. Further investigations on the effects of scattering properties can be found in [10].

Finally, Table I summarizes the volumes computed in the scenarios investigated in the previous figures using the ASCV and APVC methods. As can be noticed, results provide a rough estimation of the actual volume of the obstacle.

IV. CONCLUSIONS

In this paper, a partial multi-static UWB radar for railway crossings surveillance capable of detecting and localizing an

TABLE I
VOLUME DERIVED AFTER FOS ALGORITHM

Box volume [m^3]	Position	S	APVC [m^3]	ASVC [m^3]
5.83	in the middle	0.3	6.50	5.72
1.00	in the middle	0.3	1.45	1.58
1.00	in the corner	0.3	1.44	0.95
1.00	in the middle	0.2	1.48	1.63
0.34	in the middle	0.3	0.24	0.18

obstacle and its volume, even in static conditions, through 3D imaging has been proposed. To mitigate the ambiguity effects arising when forming the 3D image, the proposed FOS algorithm performs different scanning phases, where only a suitable subset of nodes are active at each phase and a binary hypothesis test is conducted for each 3D pixel. A realistic characterization of the environment and obstacles through ray tracing has been carried out in the numerical results to assess the 3D imaging and volume estimation capability of the system. The simulation results obtained encourage the development of the system investigated in this paper toward a future experimental validation.

ACKNOWLEDGMENT

This work is done thanks to the collaboration between Rete Ferroviaria Italiana and the University of Bologna within the project "Protezione Automatica Integrata dei Passaggi a Livello". This work was also supported in part by the Italian Ministerial PRIN project GRETA under Grant 2010WHY5PR.

REFERENCES

- [1] S. Lohmeier, R. Rajaraman, and V. Ramasami, "Development of an ultra-wideband radar system for vehicle detection at railway crossings," in *Proc. IEEE Conf. on Ultra Wideband Systems and Technologies*, May 2002, pp. 207–211.
- [2] G. Kim *et al.*, "Design of safety equipment for railroad level crossings using laser range finder," in *Proc. 9th Int. Conf. on Fuzzy Systems and Knowledge Discovery (FSKD)*, May 2012, pp. 2909–2913.
- [3] N. Fakhfakh *et al.*, "Background subtraction and 3D localization of moving and stationary obstacles at level crossings," in *Proc. 2nd Int. Conf. on Image Processing Theory Tools and Applications (IPTA)*, July 2010, pp. 72–78.
- [4] M. Chiani *et al.*, "Target detection metrics and tracking for UWB radar sensor networks," in *Proc. IEEE Int. Conf. on Ultra-Wideband (ICUWB)*, Sept 2009, pp. 469–474.
- [5] C. Le *et al.*, "Ultrawideband (UWB) radar imaging of building interior: Measurements and predictions," in *IEEE Trans. Geosci. Remote Sens.*, 2009, pp. 1409–1420.
- [6] M. Govoni *et al.*, "UWB over fiber system for railroad crossing surveillance," in *Fotonica 2015*, May 2015.
- [7] S. Nag and M. Barnes, "A moving target detection filter for an ultra-wideband radar," in *Proc. IEEE Radar Conf.*, May 2003, pp. 147–153.
- [8] H. L. V. Trees, *Detection, Estimation, and Modulation Theory: Part I*, 2nd ed. New York, NY: John Wiley & Sons, Inc., 2001.
- [9] F. Fuschini *et al.*, "Ray tracing propagation modeling for future small-cell and indoor applications: a review of current techniques," in *Radio Science*, to be published.
- [10] M. Govoni *et al.*, "Study of a UWB multi-static radar for railroad crossing surveillance," in *Proc. IEEE Int. Symp. on Antennas and Propag. and North American Radio Science Meeting*, Vancouver, British Columbia, Canada, 2015, pp. 1–2.